The Planetary Science Journal, 7:78 (9pp), 2026 April https://doi.org/10.3847/PSJ/ae523b
© 2026. The Author(s). Published by the American Astronomical Society.
OPEN ACCESS

# Morphometric Properties of the CP-21 Landing Site on the Moon at Mons Gruithuisen Gamma

Jean-Pierre Williams[1], Sarah Valencia[2,3], Kristen A. Bennett[4,5,6], Margaret E. Landis[7], Kerri L. Donaldson Hanna[8], Adrienne Dove[8], Patrick O'Brien[9], Brett W. Denevi[10], Justin Hagerty[11], Craig Hardgrove[7], Paul O. Hayne[9], Adam LaMee[8], Thomas H. Prettyman[12], Katherine A. Shirley[13], Matthew A. Siegler[14], and Jessica M. Sunshine[2]
[1] Department of Earth, Planetary, and Space Sciences, University of California, Los Angeles, CA 90095, USA; jpierre@mars.ucla.edu
[2] University of Maryland, USA
[3] NASA Goddard Space Flight Center, USA
[4] U.S. Geological Survey Astrogeology Science Center, USA
[5] Northern Arizona University, Department of Astronomy and Planetary Science, USA
[6] Northern Arizona University, Radiant Center for Remote Sensing, USA
[7] Arizona State University, USA
[8] University of Central Florida, USA
[9] University of Colorado Boulder, USA
[10] Johns Hopkins Applied Physics Laboratory, USA
[11] U.S. Geological Survey New Mexico Water Science Center, USA
[12] Planetary Science Institute, USA
[13] University of Oxford, UK
[14] University of Hawaii, USA
*Received 2025 November 24; revised 2026 March 3; accepted 2026 March 12; published 2026 April 14*

## Abstract

Characterizing terrain surface properties is an essential step in assessing the feasibility of landing successfully at a location on a planetary surface. Slopes and terrain ruggedness index (TRI) values derived from high-resolution (2 m pixel$^{-1}$) digital terrain models provided important constraints in selecting the landing site for the upcoming Payloads and Research Investigations on the Surface of the Moon program as part of the Commercial Lunar Payload Services task order CP-21 mission. The selected landing site needed to balance safety requirements with the ability to achieve the science and exploration goals of the Lunar Vulkan Imaging and Spectroscopy Explorer payload. In this study, we compare several morphometric parameters in the context of the CP-21 landing site on Mons Gruithuisen Gamma, or the Gamma dome, and quantify the information they convey about lunar surface properties to assess their utility for future landing site evaluation. TRI was found to be a useful metric for assessing landing site safety. Metrics that better decouple slope and surface roughness, the vector ruggedness measure and the standard deviation of slope, provided additional information about surface characteristics and textures such as the degree to which roughness is isotropic.

*Unified Astronomy Thesaurus concepts:* The Moon (1692); Lunar surface (974)

## 1. Introduction

An essential step in selecting a viable landing site for a planetary mission is the characterization of surface properties to assess the feasibility of landing successfully on the surface and implementing traverses for mobile platforms (e.g., R. Lorenz 2023). Past studies have used characteristic terrain properties such as slopes and surface roughness in the vicinity of past successful landed missions on the Moon (Apollo, Luna, Surveyor, Chang'E). These studies have established recommended ranges of values within which landings are known to be achievable (e.g., S. J. Lawrence et al. 2015, 2020). These ranges included slopes of $<10°$ and Terrain Ruggedness Index (TRI) values below ~0.4 using Lunar Reconnaissance Orbiter Camera (LROC) Narrow Angle Camera (NAC) digital terrain models (DTMs; 2 m pixel$^{-1}$). More recently, J. M. McCallion et al. (2024) found these recommendations held for 5 m pixel$^{-1}$ DTMs. Guidance from such studies was utilized in the selection process of the landing site for the upcoming Payloads and Research Investigations on the Surface of the Moon program (PRISM-2) task order (TO) CP-21 mission to the Gruithuisen domes region of the Moon (see J.-P. Williams et al. 2024a, 2026 for details).

The Gruithuisen domes are volcanic structures on the western margin of Mare Imbrium on the lunar nearside (Figure 1). The domes are suggested to have formed from highly viscous magmas due to their spectral signatures indicating a high silica, low iron, and titanium composition, and flanks with relatively high ~11° average slopes (M. C. Malin 1974; J. W. Head et al. 1978, J. W. Head & T. B. McCord 1978; S. D. Chevrel et al. 1999; J. J. Hagerty et al. 2006; T. D. Glotch et al. 2010; M. A. Ivanov et al. 2016). The two largest domes, Mons Gruithuisen Gamma and Mons Gruithuisen Delta, informally referred to as the Gamma and Delta domes, respectively, are ~20–30 km wide features with summit elevations ~1.8 km above the surrounding terrain. The Gamma dome has a broad, 700 m high ridge extending from its southeast corner (the Gamma Extension). Additionally, there are two smaller domes: the Northwest (NW) dome, and a more recently identified dome ~20 km southwest of the Gamma dome (N. Kumari et al. 2024). The Lunar Vulkan Imaging and Spectroscopy Explorer (Lunar-VISE) payload on CP-21 was selected as

Original content from this work may be used under the terms of the Creative Commons Attribution 4.0 licence. Any further distribution of this work must maintain attribution to the author(s) and the title of the work, journal citation and DOI.

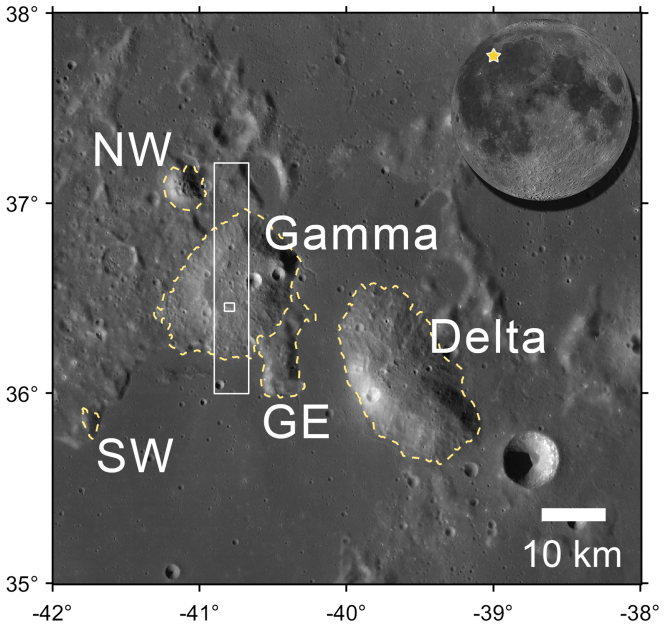


**Figure 1.** A portion of the Lunar Reconnaissance Orbiter Camera (LROC) Wide Angle Camera (WAC) morphologic global mosaic (E. J. Speyerer et al. 2011; R. V. Wagner et al. 2015) showing the Gruithuisen domes region. The yellow dashed lines outline the Gamma dome, Gamma Extension (GE), Delta dome, Northwest (NW) dome, and southwest (SW) dome. The larger white box is the location of Figure 2 and the smaller white box is the location of Figure 3. The inset lunar globe shows the location of the Gruithuisen domes on the nearside (yellow star). (NASA/GSFC/Arizona State University.)

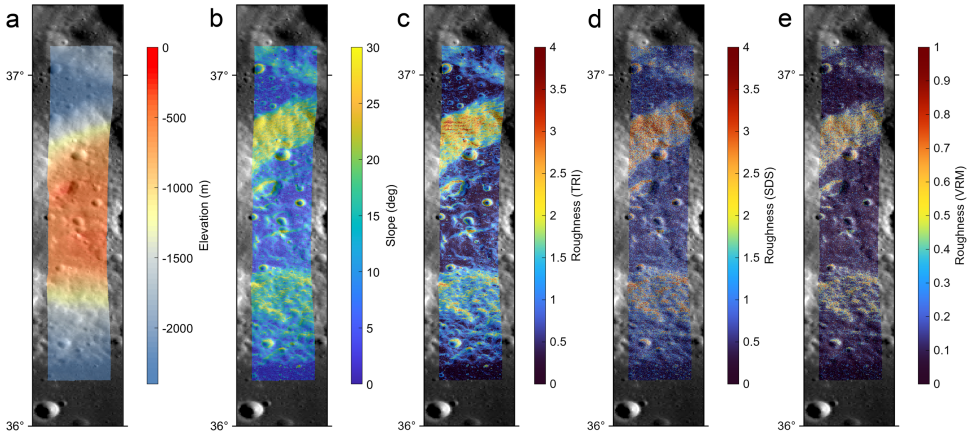


**Figure 2.** Lunar Reconnaissance Orbiter Camera (LROC) Wide Angle Camera (WAC) mosaic showing a portion of the Gamma dome overlaid with (a) elevation, (b) slope, (c) terrain ruggedness index (TRI), (d) standard deviation of slope (SDS), and (e) vector ruggedness measure (VRM) derived from the NAC Gruithuisen Domes (8) DTM (M. R. Henriksen et al. 2017). The VRM values were linearly mapped to values 0 to 1, and contrast-limited adaptive histogram equalization (S. M. Pizer et al. 1987) was applied to stretch the colors.

part of PRISM-2 with the goal of determining the composition and physical properties of dome materials and placing critical constraints on the dome formation hypotheses (K. L. Donaldson Hanna et al. 2024, 2025; C. Hardgrove et al. 2024, 2025; B. D. Byron et al. 2025).

The CP-21 landing site on Mons Gruithuisen Gamma was characterized using slopes and TRI to quantify surface properties and identify landing locations that minimize hazards to a lander (J.-P. Williams et al. 2024a, 2026). Site selection was driven by balancing landing and rover traverse safety with the ability to successfully achieve the science and exploration goals of the Lunar-VISE payload. The landing site had to not only accommodate all the attributes desired to achieve the mission goals, but also minimize hazards such as high slopes and surface roughness identified in topographic data and large boulders visible in orbital image datasets. The landing ellipse geometry is a 100 m diameter circular area. Ellipse placement was based on maximizing the area within the ellipse that fell within specific tolerances for safety. Safety requirements were not explicitly stated in the PRISM-2 call for proposals; however, the PRISM-3 call, which was released during the landing site selection process, did state sites with slopes $<10^{\circ}$ were defined as safe. Details of the landing site selection process are described in J.-P. Williams et al. (2026). In this study, we analyze several additional morphometric parameters in the context of the CP-21 landing site and compare the information they convey about lunar surface properties to assess their utility and potential applicability for future landing site evaluations.

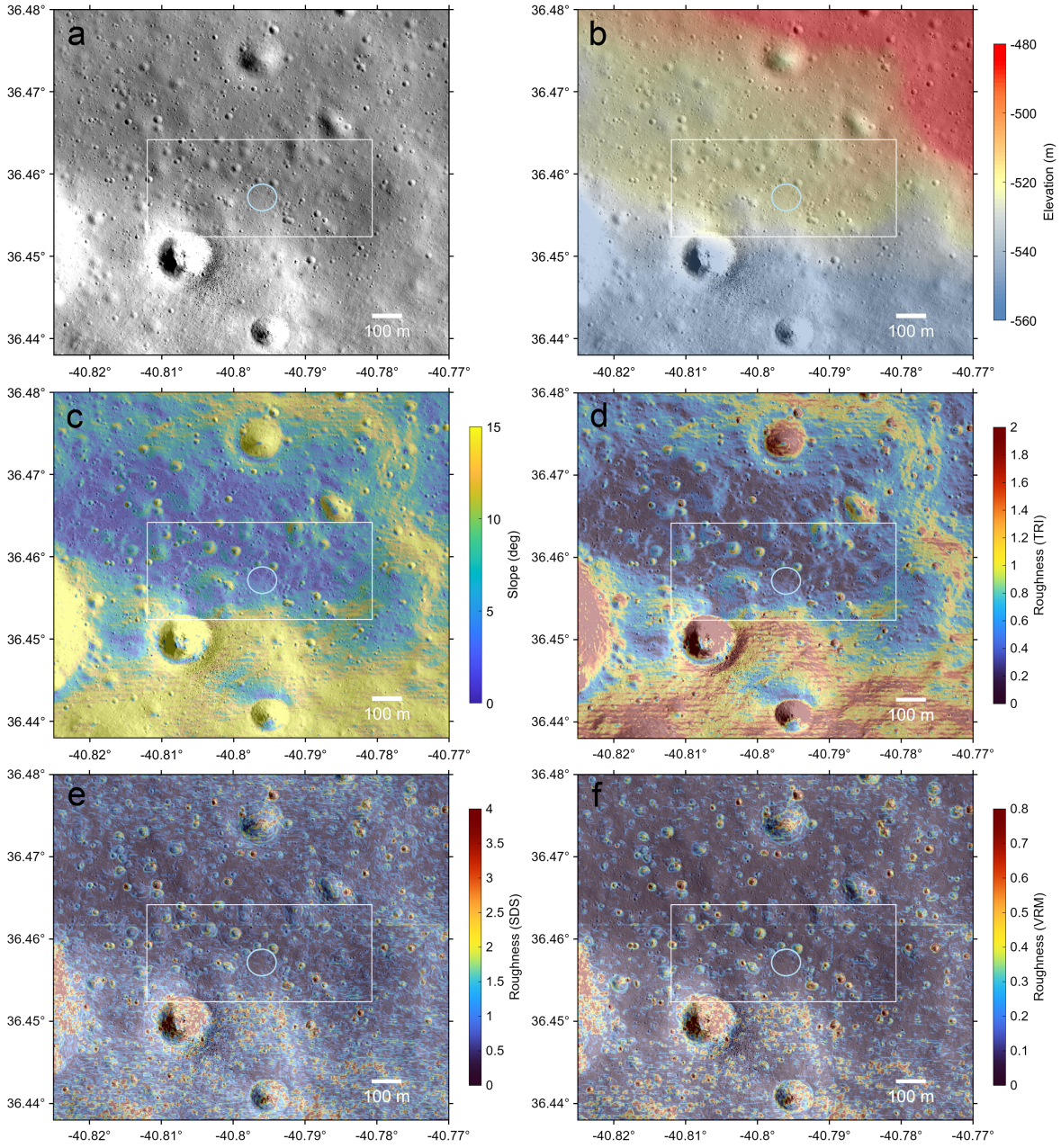


**Figure 3.** Region around the CP-21 landing area showing a portion of (a) NAC orthoimage M150783119 and colorized with (b) elevation, (c) slope, (d) TRI, (e) SDS, and (f) VRM with the 100 m diameter landing ellipse (light blue circle) and general area of operation (white rectangle) shown. The VRM values were linearly mapped to values 0–1, and contrast-limited adaptive histogram equalization (S. M. Pizer et al. 1987) was applied to stretch the colors.

## 2. Morphometric Parameters

The primary morphometric parameters utilized during the selection of the CP-21 site were slope and TRI. The TRI quantifies the variation in elevation around a central pixel within a moving window and is defined by M. F. Wilson et al. (2007) as the mean in elevation difference around the central pixel, $\frac{1}{8}\sum_{i=1}^{8}|z_i - z_\circ|$, where $z_i$ denotes the elevations of the individual cells surrounding the central cell $z_o$. Areas will have elevated TRI values if they are on either sloped surfaces or surfaces that are rough at the length scale of the DTM. Either of these situations will create variations in elevation within the window. This means that TRI generally correlates with slope to a high degree. J.-P. Williams et al. (2024b) showed that TRI and slope are strongly correlated within the Faustini permanently shadowed region.

Other morphometric parameters may be favorable if a decoupling of surface roughness and slope is desired. Here we explore two additional terrain indices that have recently been used to characterize surface roughness on the Moon: vector ruggedness measure (VRM) and the standard deviation of slope (SDS), both of which quantify variations in elevation gradients. SDS quantifies the variation in gradients (K. L. Frankel & J. F. Dolan 2007) and VRM the dispersion of surface normal vectors (R. D. Hobson 1972;

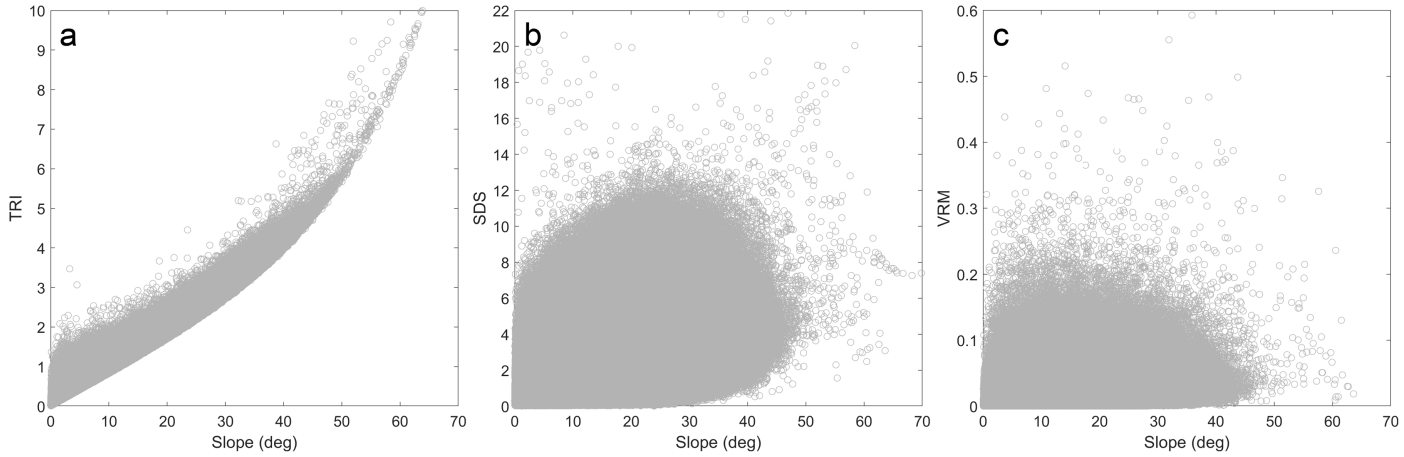


**Figure 4.** Scatter plots of the slope and (a) TRI, (b) SDS, and (c) VRM derived from the NAC Gruithuisen Domes (8) DTM.

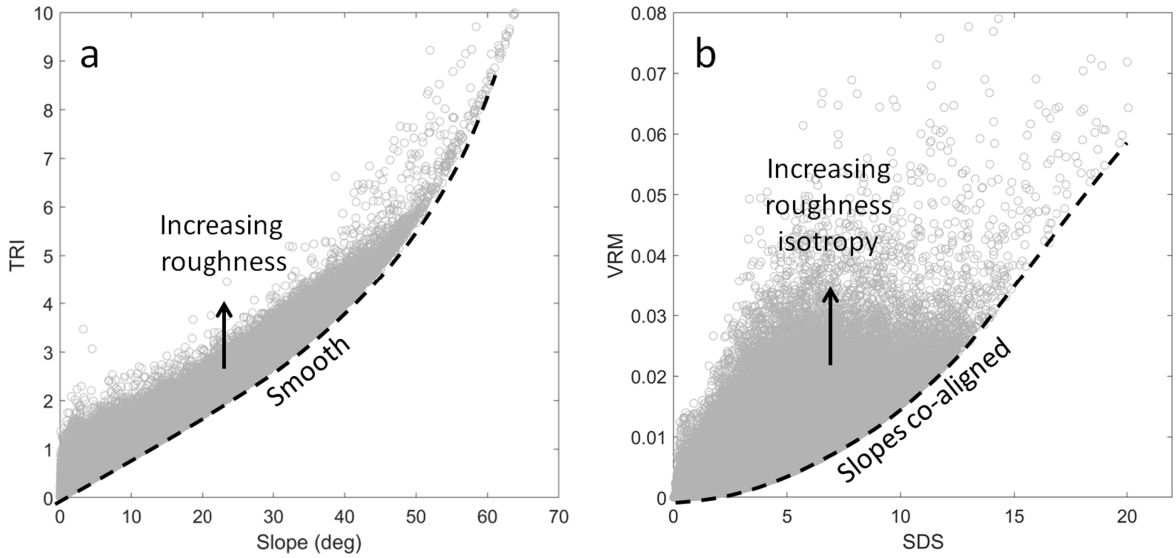


**Figure 5.** Scatter plots of (a) slope and TRI, and (b) SDS and VRM. Dashed curves are envelopes defined by terrain configurations that minimize (a) TRI values for a given slope, or (b) VRM values for a given SDS. These terrain configurations correspond to (a) smooth surfaces, or (b) roughness with coaligned slopes, and departures from these curves suggest increasing roughness or roughness isotropy, respectively.

J. M. Sappington et al. 2007) of elements within a moving window. SDS is computed as

$$SDS = \sqrt{\frac{\sum_{i=1}^{n}(m_i - \bar{m})^2}{n}}, \quad (1)$$

where $\bar{m}$ is the mean slope, $m_i$ are the slopes of the individual cells, and $n$ is the number of cells within the window. VRM is defined as

$$VRM = 1 - \frac{|r|}{n}, \quad (2)$$

where $|r|$ is the magnitude of the resultant vector of the surface normals:

$$r = \sqrt{\left(\sum x_i\right)^2 + \left(\sum y_i\right)^2 + \left(\sum z_i\right)^2}, \quad (3)$$

and $x_i = \sin(m_i)\cdot\sin(\alpha_i)$, $y_i = \sin(m_i)\cdot\cos(\alpha_i)$, and $z_i = \cos(m_i)$ where $\alpha_i$ is the azimuthal angle of the slope for each cell.

If the surface within a window is sloped, but perfectly smooth at the DTM length scale, SDS and VRM will be zero as there will be no variation in elevation gradients, and the normal vectors will remain aligned, i.e., no dispersion of the normal vectors. However, TRI could be large as the elevations will vary due to the slope (see Section 4 below). An alternate approach to account for slope is to detrend TRI by subtracting a best-fit plane to the moving window (M. K. Barker et al. 2023; L. O. Magaña et al. 2024).

## 3. Morphometric Parameters of the CP-21 Landing Site

Previous studies have used SDS or VRM parameters to quantify surface roughness variation in the lunar polar regions (A. N. Deutsch et al. 2021; S. Moon et al. 2021; J.-P. Williams et al. 2024b). To provide additional information about landing site surface characteristics, we compare VRM and SDS with slope and TRI in the CP-21 landing site region. We have

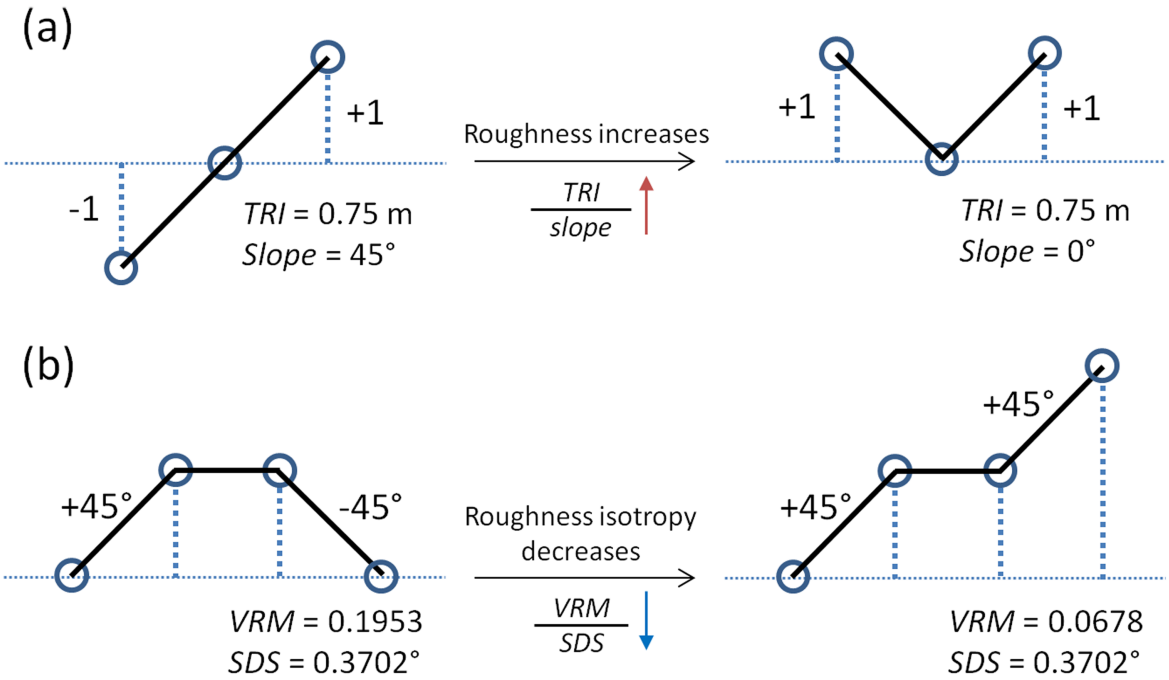


**Figure 6.** Idealized terrain configurations demonstrating how morphometric parameters vary relative to each other for (a) TRI and slope, and (b) VRM and SDS. (a) A smooth surface sloped at 45° (left) and a rough, flat surface represented as a notch with 45° sloped surfaces facing toward each other (right). (b) A bump with 45° sloped surfaces on either side facing away from each other (left) and a step with 45° sloped surfaces on either side facing in the same direction (right).

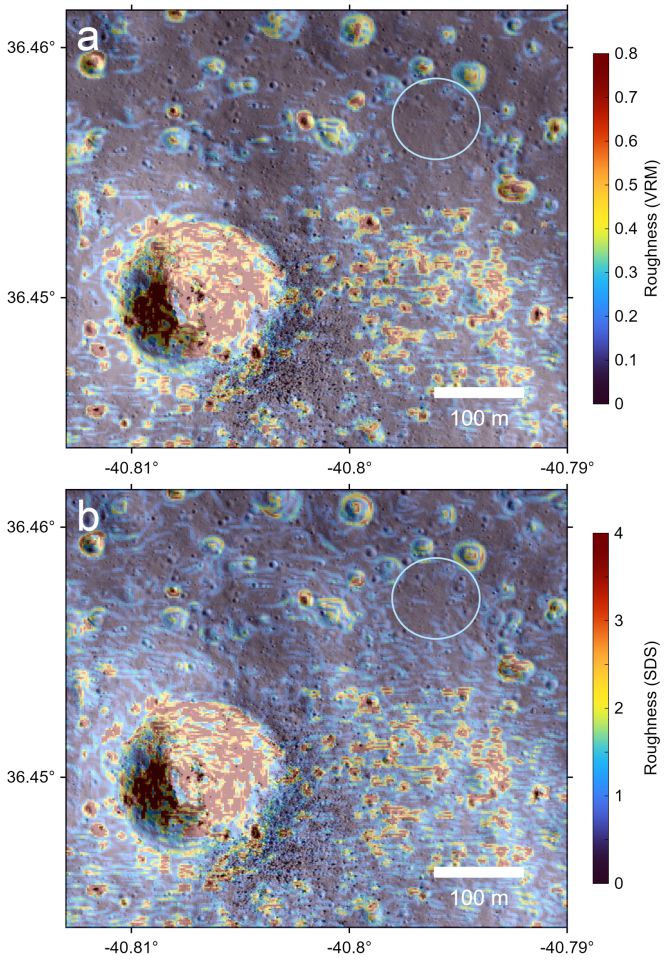


**Figure 7.** A portion of NAC orthoimage M150783119 showing the landing and rover operations area, including the landing ellipse (light blue circle) and the boulder field source crater, formally named Mareta (lower left), superposed with (a) VRM and (b) SDS.

generated these morphometric parameters for the 2 m pixel$^{-1}$ LROC NAC-derived Gruithuisen Domes (8) DTM, which covers the portion of the Gamma dome containing the CP-21 landing site (Figures 1–3) with a relative vertical and horizontal precision smaller than the pixel scale (M. R. Henriksen et al. 2017). Slopes were determined using Horn's algorithm (B. K. Horn 1981), a commonly used method that has been shown to perform well against test surfaces (K. H. Jones 1998). This method is defined for a 3 × 3 sampling window, or kernel. For comparison, all parameters were calculated on a pixel-by-pixel basis using a 3 × 3 sampling grid with an effective baseline of 4 m. Using a 3 × 3 window preserves the maximum detail for the smallest-scale topographic features, which is desirable for assessing landing safety and rover traversability. Larger windows will have a smoothing effect, reducing small-scale topographic detail.

Scatter plots of slope versus TRI, SDS, and VRM show how SDS and VRM successfully decouple surface ruggedness from slope relative to TRI, which is highly correlated with slope for the area covered by the DTM (Figure 4). This is apparent in Figure 3, showing these parameters in the region of the CP-21 landing site. The landing site is near the edge of a bench in the topography near the peak of the Gamma dome (36.45715°N, 319.20398°E; Figure 3). Large changes in slope surrounding the bench of topography have elevated TRI values that result from higher slopes at the dome edge and the step in elevation from the bench toward the summit (Figure 3(c)). SDS and VRM values show minimal sensitivity to these inflections in slope, but rather highlight smaller wavelength features due to localized (meter-scale) variation in surface topography such as impact craters (Figures 3(d) and (f)).

## 4. Interpretation of Morphometric Parameters

While TRI has a strong correlation with slope, there is some variation in the parameter for a given slope (Figure 5(a)). For

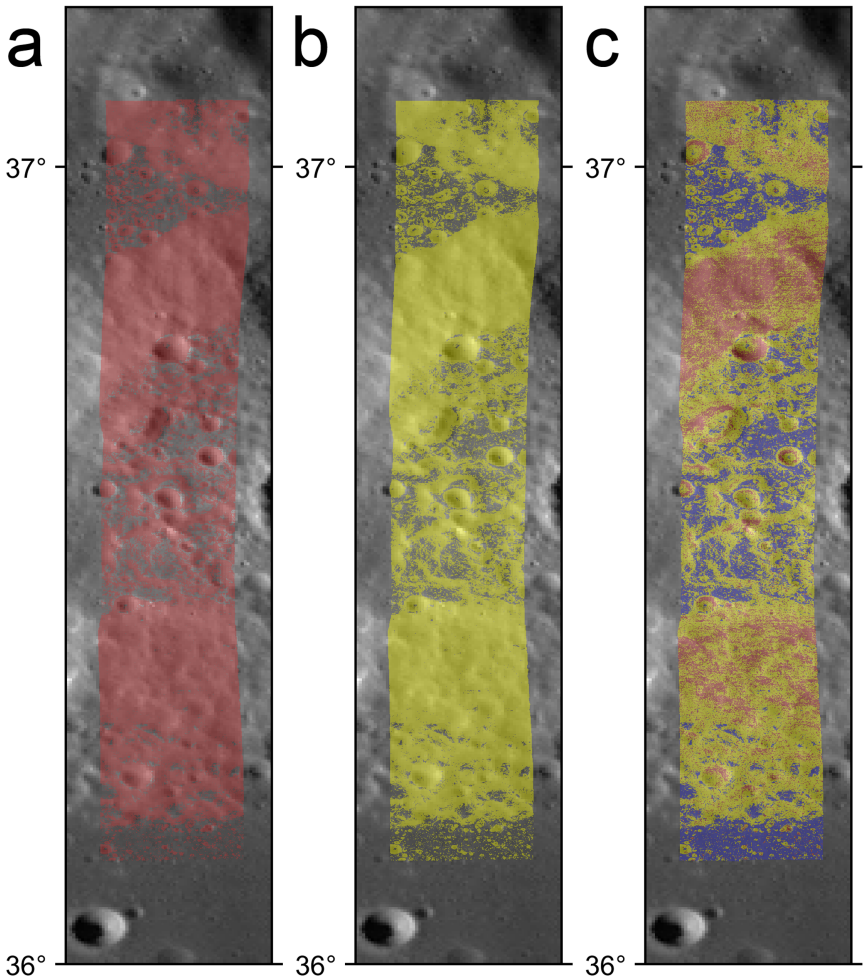


**Figure 8.** Terrain identified as (a) sloped (>5°, red), (b) high TRI (>0.4 m, yellow), and (c) sloped/flat and smooth/rough, defined using slopes, SDS, and VRM parameter thresholds as described in the text for the Gruithuisen domes, where red = sloped and rough, yellow = sloped and smooth, and blue = flat and smooth.

the idealized case of a perfectly smooth surface without small undulations within the 3 × 3 window, TRI will be directly coupled with slope. If the smooth surface is tilted such that the slope is doubled, the value of TRI will double as the mean in elevation difference around the central pixel will double. However, if small variations in elevation are introduced, i.e., the surface is roughened, TRI can increase relative to the slope. For example, a smooth surface tilted at 45° will have TRI = 0.75 m. However, if the surface has a notch with edges at the same elevation, but the center is at a lower elevation such that there are two faces sloped at 45° toward each other, the slope will be 0° for the 3 × 3 window, but TRI will remain 0.75 m (Figure 6(a)). This suggests that a smooth surface represents the minimum TRI configuration for a given slope and explains the sharp boundary at the lower edge of the distribution of markers in the scatter plot in Figure 4(a) and highlighted in Figure 5(a). The departures of points above that boundary are surfaces with increased roughness.

Since SDS and VRM quantify variations in elevation gradients, rather than variations in elevations as slope and TRI do, they highlight roughness within the 3 × 3 window regardless of how the overall window is tilted. Any correlation with slope will be geologic, i.e., if sloped surfaces are also preferentially rough and not inherent in the parameters. Terrain with high SDS values is generally observed to have high VRM values, but VRM and SDS are not identically correlated as there is a fair amount of variation between these values (Figure 5(b)). A sharp, well-defined boundary is also observed in the scatter plot of these two parameters, as was observed for slope versus TRI. This suggests that a topographic configuration also exists that minimizes VRM relative to SDS.

VRM contains additional information about slope orientation as it will be influenced by the slope azimuth angle, while SDS is agnostic to slope direction or sign. This can be seen by comparing two idealized examples. The first case is an axisymmetric bump extending in the $y$-direction to form a ridge such that $\sum y_i = 0$ in Equation (3) can be ignored. The bump is a central flat cell with 45° slopes oriented in opposite directions on either side (Figure 6(b)). The second case is an axisymmetric step, again oriented along the $y$-direction, with 45° slopes on either side of the central cell, but now oriented in the same direction with the same sign (Figure 6(b)). In both cases, SDS = $0\overset{\circ}{.}3702$, as the sums of the slope magnitudes in both cases are the same. However, VRM = 0.1953 in the first case, but is 0.0678 in the second case. This results from the change in the sign of the slopes in the first case resulting in the sum of the $x_i$ values canceling out and only the $z_i$ term contributing to the resultant vector, while in the second case, the sum of $x_i$ values is nonzero. This suggests that VRM is minimized relative to SDS when slopes are coaligned with a homogeneous distribution of slope azimuth angles and all horizontal components of slope add to the resultant vector.

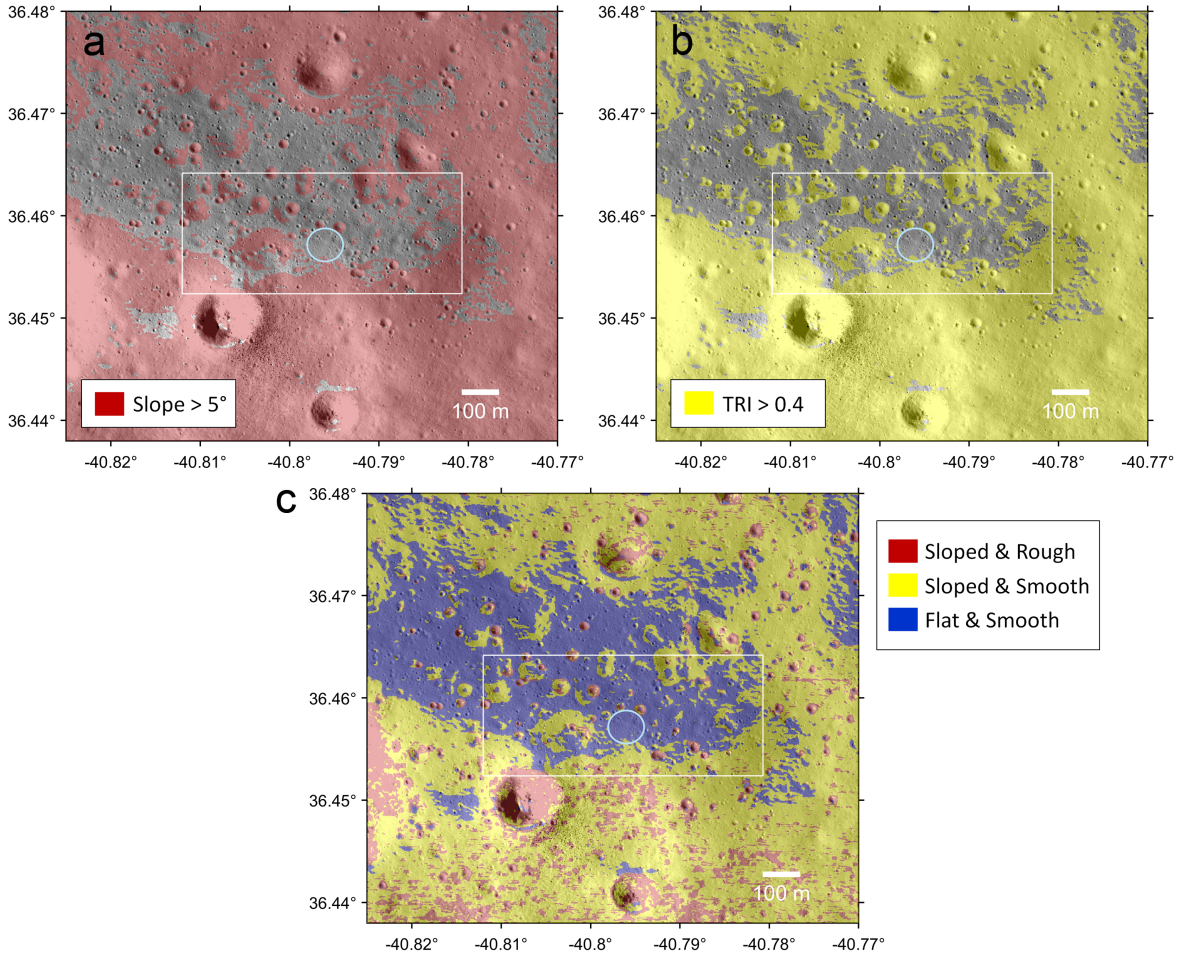


**Figure 9.** Terrain identified as (a) sloped (>5°), (b) high TRI (>0.4 m), and (c) sloped/flat and smooth/rough, defined using slopes, SDS, and VRM parameter thresholds as described in the text.

VRM will increase with increasing azimuth angle heterogeneity, which will lead to an increase in the horizontal components of slope subtracting from each other in the resultant vector, thereby reducing the resultant vector magnitude and increasing VRM.

Differences between VRM and SDS therefore can be used to infer to what degree roughness is isotropic. Figure 7 shows VRM and SDS values around the landing and rover operational area, including a dense boulder field and source crater (see J.-P. Williams et al. 2024a, 2026 for details of the landing area). Both VRM and SDS values are elevated in and around impact craters large enough to be resolved in the DTM, while the intercrater areas are elevated in SDS relative to VRM. Both parameters show areas with elevated isotropic roughness, but SDS is also elevated where roughness is anisotropic (slopes with preferential direction). The elevated SDS values in the intercrater areas reveal a texture with a preferential north–south slope orientation (predominantly seen as cyan colors in Figure 7(b)) that is not as apparent in VRM, since VRM is more sensitive to isotropic roughness.

## 5. Characterization of the CP-21 Landing Area

All these morphometric parameters can be used as terrain discriminators to map areas as generally safe or hazardous for landing successfully. Here, we define terrains as flat or sloped based on slopes being either less than or greater than 5°, and smooth or rough where we have defined smooth surfaces having VRM $< 0.0007$ and SDS $< 1.5°$. While the PRISM-3 call stated that slopes as high as 10° were deemed safe, attempts were made to minimize slopes >5° within the landing ellipse during the selection process (J.-P. Williams et al. 2024a, 2026). Slopes >5° were also found to generally correspond to TRI values $> 0.4$ m. The VRM and SDS values used to define a "smooth" surface were determined from visual inspection of NAC images, where surfaces with greater values were observed to correspond reasonably well to terrain features that could challenge landing safety. While these values are somewhat ad hoc, additional characterization of these parameters around past successful landing sites, as was done for slope and TRI (S. J. Lawrence et al. 2015, 2020; J. M. McCallion et al. 2024), could provide additional guidance on applying these parameters to access landing site safety.

Terrain categories were defined for the LROC NAC Gruithuisen Domes (8) DTM (Figures 8 and 9). Flat and smooth surfaces (slopes <5° and VRM $< 0.0007$, SDS $< 1.5°$) comprise 21% of the DTM area, while sloped/smooth and sloped/rough surfaces were 55% and 23% of the area, respectively. Flat/rough surfaces were <1%, meaning rough surfaces are nearly always found on slopes >5°.

The final placement of the landing ellipse involved a best effort to minimize the area within the ellipse with slopes >5°

**Table 1**
Landing Ellipse Characteristics

| Parameter | Mean ± Std. Dev. | Percent "Safe"[a] |
|---|---|---|
| Slope (deg) | 2.79 ± 1.35 | 94.5 |
| TRI (m) | 0.25 ± 0.11 | 90.9 |
| VRM | $8.5 \times 10^{-5} \pm 0.1 \times 10^{-4}$ | 99.6 |
| SDS (deg) | 0.43 ± 0.26 | 99.1 |

**Note.**
[a] Slopes <5°; TRI < 0.4 m; VRM < 0.007; SDS < 1.°5.

and TRI >0.4 m (J.-P. Williams et al. 2024a, 2026). We note that no location studied provided an area large enough to place an ellipse with 100% of the area below these thresholds that also allowed for all the required and desired site attributes to be met, as described in J.-P. Williams et al. (2024a, 2026). Figure 9 shows the landing ellipse and rover operational area relative to the slope (Figure 9(a)) and TRI (Figure 9(b)) thresholds, and the terrain categories (Figure 9(c)). Nearly the entire ellipse falls within an area that is "safe," with the majority of the ellipse in terrain that meets our definition of "flat and smooth." The mean morphometric parameter values for the ellipse are summarized in Table 1, along with the percentage of the ellipse that is deemed "safe" based on our parameter thresholds.

## 6. Conclusions

Morphometric parameters provide critical information about the surface topography that can aid in evaluating the safety of a landing ellipse. While slope describes how terrain deviates from a horizontal surface with respect to the local gravitational normal, VRM and SDS quantify how the terrain deviates from a smooth surface, sloped or otherwise. TRI captures information about both. TRI is potentially more inclusive of potentially hazardous terrain conditions than any of the other parameters alone, and therefore, as a singular metric, is a useful terrain discriminator for landing site safety. VRM and SDS would be useful metrics in an application where decoupling slope and surface roughness is necessary. For the CP-21 landing area, we found TRI >0.4 m encompassed all surfaces with slopes >5° and nearly all surfaces with either VRM and/or SDS values that we considered indicative of rough surfaces. However, we have only explored these parameters for a single NAC DTM centered on the CP-21 landing site. This DTM was the highest resolution available and was analyzed as part of the landing site selection process (J.-P. Williams et al. 2024a, 2026). For CP-21, TRI provided a useful metric in selecting the placement of a landing ellipse. Details about terrain properties provided by VRM and SDS further validate the choice and confirm the location as being optimal. This suggests that TRI is a comprehensive initial choice for landing site downselection, and that additional metrics can give supporting insight during further study.

## Acknowledgments

Funding for this work was made possible by the NASA PRISM program through cooperative agreement number 80NSSC22M0303. All data used in the study are publicly available, or derived from publicly available data as described in Section 2, from the following sources: LROC WAC morphologic global mosaic (https://wms.lroc.asu.edu/lroc/view_rdr/WAC_GLOBAL); LROC NAC DTM and orthophoto (https://wms.lroc.asu.edu/lroc/view_rdr/NAC_DTM_GRUITHUISE8). Derived slope and TRI maps are available in a public archive (J.-P. Williams et al. 2025). Any use of trade, firm, or product names is for descriptive purposes only and does not imply endorsement by the US Government. We wish to thank two anonymous reviewers who provided helpful and constructive comments that improved the manuscript.

## ORCID iDs

Jean-Pierre Williams https://orcid.org/0000-0003-4163-2760
Margaret E. Landis https://orcid.org/0000-0001-7321-2272
Patrick O'Brien https://orcid.org/0000-0002-3212-7802
Paul O. Hayne https://orcid.org/0000-0003-4399-0449
Katherine A. Shirley https://orcid.org/0000-0003-0669-7497
Jessica M. Sunshine https://orcid.org/0000-0002-9413-8785

## References

Barker, M. K., Mazarico, E., Neumann, G. A., et al. 2023, A New View of the Lunar South Pole from the Lunar Orbiter Laser Altimeter (LOLA), PSJ, 4, 183
Byron, B. D., Donaldson Hanna, K. L., Dove, A., et al. 2025, MER Mini-TES Observations of Rover Wheel Tracks: Application to Lunar-VISE at Mons Gruithuisen Gamma, LPSC, 56, 2480
Chevrel, S. D., Pinet, P. C., & Head, J. W. 1999, Gruithuisen Domes Region: A Candidate for an Extended Nonmare Volcanism Unit on the Moon, JGRE, 104, 16515
Deutsch, A. N., Heldmann, J. L., Colaprete, A., Cannon, K. M., & Elphic, R. C. 2021, Analyzing Surface Ruggedness Inside and Outside of Ice Stability Zones at the Lunar Poles, PSJ, 2, 213
Donaldson Hanna, K. L., Benavente, J., Bennett, K., et al. 2024, Lunar-VISE In Situ Investigation of Mons Gruithuisen Gamma, LPSC, 55, 2170
Donaldson Hanna, K. L., Benavente, J., Bennett, K., et al. 2025, Update on the Lunar-VISE Investigation of Mons Gruithuisen Gamma, LPSC, 56, 2213
Frankel, K. L., & Dolan, J. F. 2007, Characterizing Arid Region Alluvial Fan Surface Roughness with Airborne Laser Swath Mapping Digital Topographic Data, JGRE, 112, F02025
Glotch, T. D., Lucey, P. G., Bandfield, J. L., et al. 2010, Highly Silicic Compositions on the Moon, Sci, 328, 1510
Hagerty, J. J., Lawrence, D. J., Hawke, B. R., et al. 2006, Refined Thorium Abundances for Lunar Red Spots: Implications for Evolved, Nonmare Volcanism on the Moon, JGRE, 111, E06002
Hardgrove, C., Prettyman, T., Johnson, E. B., et al. 2024, The Lunar-VISE Gamma-ray and Neutron Spectrometer: In-situ Elemental Measurements of the Gruithuisen Domes, LPSC, 55, 2258
Hardgrove, C., Prettyman, T., Johnson, E. B., et al. 2025, Development and Qualification of the Lunar-VISE Gamma-ray and Neutron Spectrometers (GRNS), LPSC, 56, 2283
Head, J. W., Hess, P. C., & McCord, T. B. 1978, Geologic Characteristics of Lunar Highland Volcanic Domes (Gruithuisen and Mairan Region) and Possible Eruption Conditions, LPI, 9, 488
Head, J. W., & McCord, T. B. 1978, Imbrian-aged Highland Volcanism on the Moon: The Gruithuisen and Mairan Domes, Sci, 199, 1433
Henriksen, M. R., Manheim, M. R., Burns, K. N., et al. 2017, Extracting Accurate and Precise Topography from LROC Narrow Angle Camera Stereo Observations, Icar, 283, 122
Hobson, R. D. 1972, Surface Roughness in Topography: Quantitative Approach, in Spatial Analysis in Geomorphology, ed. R. J. Chorley (Harper and Row), 221
Horn, B. K. 1981, Hill Shading and the Reflectance Map, IEEEP, 69, 14
Ivanov, M. A., Head, J. W., & Bystrov, A. 2016, The Lunar Gruithuisen Silicic Extrusive Domes: Topographic Configuration, Morphology, Ages, and Internal Structure, Icar, 273, 262
Jones, K. H. 1998, A Comparison of Algorithms Used to Compute Hill Slope as a Property of the DEM, CG, 24, 315

Kumari, N., Glotch, T. D., Williams, J. P., et al. 2024, Extended Silicic Volcanism in the Gruithuisen Region—Revisiting the Composition and Thermophysical Properties of Gruithuisen Domes on the Moon, PSJ, 5, 132
Lawrence, S. J., Stopar, J. D., Gruener, J. E., et al. 2020, Morphologic Parameters for Successful Lunar Landing Sites, LPSC, 51, 2579
Lawrence, S. J., Stopar, J. D., Jolliff, B. L., Speyerer, E. J., & Robinson, M. S. 2015, Lunar Surface Traverse and Exploration Planning: What Makes a "Good" Landing Site?, LPICo, 1863, 2074
Lorenz, R. 2023, Slopes on Titan and Application to Spacecraft Landing Safety, P&SS, 235, 105745
Magaña, L. O., Prem, P., Deutsch, A. N., et al. 2024, Surface Roughness at the Moon's South Pole: The Influence of Condensed Volatiles on Surface Roughness at the Moon's South Pole, PSJ, 5, 30
Malin, M. C. 1974, Lunar Red Spots: Possible Pre-mare Materials, E&PSL, 21, 331
McCallion, J. M., Lawrence, S. J., & Stopar, J. D. 2024, Morphometric Characterization of Lunar Landing Sites, LPSC, 55, 2273
Moon, S., Paige, D. A., Siegler, M. A., & Russell, P. S. 2021, Geomorphic Evidence for the Presence of Ice Deposits in the Permanently Shadowed Regions of Scott-E Crater on the Moon, GeoRL, 48, e2020GL090780
Pizer, S. M., Amburn, E. P., Austin, J. D., et al. 1987, Adaptive Histogram Equalization and its Variations, CVGIP, 39, 355
Sappington, J. M., Longshore, K. M., & Thompson, D. B. 2007, Quantifying Landscape Ruggedness for Animal Habitat Analysis: A Case Study Using Bighorn Sheep in the Mojave Desert, JWMan, 71, 1419
Speyerer, E. J., Robinson, M. S., Denevi, B. W. & LROC Science Team 2011, Lunar Reconnaissance Orbiter Camera Morphological Map of the Moon, LPSC, 42, 2387
Wagner, R. V., Speyerer, E. J., Robinson, M. S. & LROC Team 2015, New Mosaicked Data Products from the LROC Team, LPSC, 46, 1473
Williams, J.-P., Landis, M., Bennett, K., et al. 2025, Data for "Lunar-VISE Landing Site Selection and Characterization at Mons Gruithuisen Gamma," v1, Zenodo, doi:10.5281/zenodo.15778239
Williams, J.-P., Landis, M., Bennett, K., et al. 2026, Lunar-VISE Landing Site Selection and Characterization at Mons Gruithuisen Gamma, PSJ, submitted
Williams, J.-P., Landis, M. E., Bennett, K. A., et al. 2024a, Lunar-VISE: Landing Site Selection and Characterization at Gruithuisen Domes, LPSC, 55, 1688
Williams, J.-P., Mahanti, P., Robinson, M. S., et al. 2024b, The Faustini Permanently Shadowed Region on the Moon, PSJ, 5, 209
Wilson, M. F., O'Connell, B., Brown, C., Guinan, J. C., & Grehan, A. J. 2007, Multiscale Terrain Analysis of Multibeam Bathymetry Data for Habitat Mapping on the Continental Slope, MarGe, 30, 3